

# Chapter 5

## Evolution of circumstellar discs in young star forming regions

F. Concha-Ramírez; S. Portegies Zwart; M.J.C. Wilhelm

In preparation for submission to Monthly Notices of the Royal Astronomical Society

### Abstract

The evolution of circumstellar discs is highly influenced by their surroundings, in particular by external photoevaporation due to nearby stars and dynamical truncations. The impact of these processes on disc populations depends on the dynamical evolution of the star forming region. Here we implement a simple model of molecular cloud collapse and star formation to obtain primordial positions and velocities of young stars and follow their evolution in time, including their circumstellar discs. Our disc model takes into account viscous evolution, internal and external photoevaporation, dust evolution, and dynamical truncations. The disc evolution is resolved simultaneously with the star cluster dynamics and stellar evolution. Our results show that an extended period of star formation allows for massive disks to survive for several million years. This could explain massive discs surviving in regions of high UV radiation.

## 1 Introduction

Circumstellar discs are a natural consequence of the star formation process, and emerge within the first  $10^4$  yr after star formation (Williams & Cieza, 2011). The star formation environment, rich in gas and newly-formed stars, can greatly affect the evolution of the discs. The imprints that this environment will leave on the young discs have important repercussions on their potential to form planets and on the configurations of the planetary systems that eventually develop.

There are several ways in which the environment can influence the evolution of circumstellar discs. Close encounters between circumstellar discs and stellar fly-bys can affect the size, mass, and surface density of the discs. Close encounters can remove mass from the outskirts of the discs, decreasing both their mass and radius (e.g. Clarke & Pringle, 1991, 1993; Pfalzner et al., 2005b; Breslau et al., 2014; Vincke et al., 2015; Vincke & Pfalzner, 2016; Portegies Zwart, 2016; Vincke & Pfalzner, 2018; Cuello et al., 2018; Winter et al., 2018a; Concha-Ramírez et al., 2019a). Several numerical implementations of this process have shown that close encounters can lead to a hardening of the discs surface density (Rosotti et al., 2014), the formation of spiral arms and other structures (Pfalzner, 2003; Pfalzner et al., 2005a), accretion bursts onto the host star (Pfalzner et al., 2008), and exchange of mass between discs (Pfalzner et al., 2005b; Jílková et al., 2016). Observational evidence for the effects of stellar fly-bys has been presented in several studies. Cabrit et al. (2006) study the  $\sim 600$  au trailing “tail” in the disc of RW Aur A and suggest that it might have been caused by a recent fly-by. Observations by Rodriguez et al. (2018) reveal newly-detected tidal streams in RW Aur A and they propose that these might be the result of many subsequent close encounters. Reche et al. (2009) suggest that the spiral arms observed in the disc of the triple star system HD 141569 might be the result of a fly-by. Winter et al. (2018c) simulate the disc around DO Tau, which presents a tidal tail, and argue that this shape could have been caused by a close encounter with the nearby triple system HV Tau. There is also evidence that the young disc of the solar system was affected by such an encounter. The sharp edge of the solar system at  $\sim 30$  au could be a sign that a passing star truncated its early disc (Breslau et al., 2014; Punzo et al., 2014). The highly eccentric and inclined orbits of the *Sednitos*, a group of 13 detected planetoids in the outskirts of the solar system, suggest they might have been captured from the disc of a passing nearby star (Jílková et al., 2015).

Another mechanism that can alter the evolution of circumstellar discs is photoevaporation. Photoevaporation is the process in which high energy photons heat the disc surface, causing them to evaporate. The

source of these photons can be the host star (internal photoevaporation) or bright stars in the vicinity (external photoevaporation). Photoevaporation is driven by far ultraviolet (FUV), extreme ultraviolet (EUV), and X-ray photons (Johnstone et al., 1998; Adams et al., 2004). The effects of internal and external photoevaporation over circumstellar discs are rather distinct. Internal photoevaporation can clear areas of the disc at specific disc radii, causing the opening of gaps (Gorti et al., 2009; Gorti & Hollenbach, 2009; Owen et al., 2010; Font et al., 2004; Fatuzzo & Adams, 2008; Hollenbach et al., 2000). External photoevaporation can remove mass from all over the disc surface, but the outer regions of the discs are more vulnerable because the material is less strongly bound to the host star (Johnstone et al., 1998; Adams et al., 2004).

Observational evidence of external photoevaporation was first obtained through the imaging of evaporating discs in the Orion nebula (O’dell & Wen, 1994; O’dell, 1998). These objects, now known as ‘proplyds’, are circumstellar discs immersed in the radiation fields of nearby stars. Their cometary tail-like structure reveals the undergoing mass loss. Subsequent observations of the region showed circumstellar disc masses decrease when close to massive stars. This effect has been observed in several regions such as the Trapezium cluster (e.g. Vicente & Alves, 2005; Eisner & Carpenter, 2006; Mann et al., 2014), the Orion Nebula Cluster (e.g. Mann & Williams, 2010; Eisner et al., 2018), Cygnus OB2 (Guarcello et al., 2016), NGC 1977 (Kim et al., 2016), NGC 2244 (Balog et al., 2007), Pismis 24 (Fang et al., 2012), NGC 2024 (van Terwisga et al., 2020),  $\sigma$  Orionis (Ansdell et al., 2017), and  $\lambda$  Orionis (Ansdell et al., 2020). Younger and low-mass star forming regions such as Lupus, Taurus, Ophiuchus, and the Orion Molecular Cloud 2 have higher average disc masses than denser regions such as the Orion Nebula Cluster (Eisner et al., 2008; Ansdell et al., 2016; Eisner et al., 2018; van Terwisga et al., 2019). van Terwisga et al. (2020) present the discovery of two distinct disc populations, in terms of mass, in the NGC 2024 region. The discs to the east of the region are embedded in a dense molecular ridge and are more massive than the discs outside the ridge, which are also closer to two OB type stars. They propose that the difference in masses is caused by the eastern population being protected from the radiation of nearby massive star IRS 1.

Several models have shown that external photoevaporation is efficient in depleting disc masses on timescales much shorter than their estimated lifetimes of  $\sim 10$  Myr (e.g. Scally & Clarke, 2001; Adams et al., 2006; Fatuzzo & Adams, 2008; Haworth et al., 2016), even in low radiation fields (Facchini et al., 2016; Kim et al., 2016; Haworth et al., 2017). Because external photoevaporation is caused by massive stars in the vicinity of the discs, the extent of its effects depends on the density of the stellar region and the number of massive stars in the surroundings. Even in high density regions ( $N_* \gtrsim 10^4 \text{ pc}^{-3}$ ) the disc mass-loss rates caused by external photoevaporation are orders of magnitude higher than those caused by dynamical truncations (Winter et al., 2018b, 2019b; Concha-Ramírez et al., 2019b). Concha-Ramírez et al. (2020) show that, in regions of local stellar densities  $N_* > 100 \text{ pc}^{-3}$ , external photoevaporation can evaporate up to 90% of circumstellar discs within 2.0 Myr. For regions of density  $\sim 10 \text{ M}_\odot \text{ pc}^{-3}$ ,  $\sim 60\%$  of discs are evaporated within the same timescale. Winter et al. (2020) model a region comparable to the central molecular zone of the Milky Way (surface density  $\Sigma_0 = 10^3 \text{ M}_\odot \text{ pc}^{-2}$ ) and find that external photoevaporation destroys 90% of circumstellar discs within 1.0 Myr. In regions of lower density ( $\Sigma_0 = 12 \text{ M}_\odot \text{ pc}^{-2}$ ) they find a mean disc dispersion timescale of 3.0 Myr. Similar results are obtained by Nicholson et al. (2019) who find that external photoevaporation destroys 50% of discs within 1.0 Myr in regions of density  $\sim 100 \text{ M}_\odot \text{ pc}^{-3}$ , and within 2.0 Myr in regions of density  $\sim 10 \text{ M}_\odot \text{ pc}^{-3}$ .

While observational and numerical evidence indicate that disc masses decrease with increasing stellar density, massive discs are still observed in high density regions. In particular, there are discs in the ONC whose masses are much higher than other discs in the proximity of the massive star  $\theta^1$  Ori C. If the discs are coeval with  $\theta^1$  Ori C they should have already been dispersed by external photoevaporation, unless they were extraordinarily massive to begin with ( $M_{\text{disc}} \gtrsim 1 \text{ M}_\odot$ ). Otherwise,  $\theta^1$  Ori C would have to be considerably younger than the ONC average ( $\lesssim 0.1$  Myr) for these discs to have survived. This is known as the ‘proplyd lifetime problem’. Störzer & Hollenbach (1999) propose that these discs are currently passing by the centre of the region, but have spent most of their lifetimes far enough from it to be protected from the radiation. Scally & Clarke (2001) model external photoevaporation on a cluster similar to the ONC and find that the necessary orbits proposed by Störzer & Hollenbach (1999) are not dynamically plausible in such a region. Winter et al. (2019b) revisit the problem and propose a solution to describe why these discs exist. The solution consists of a combination of factors: different eras of star formation allow for massive discs to be around stars that are younger than the average of the ONC population; stars forming in subvirial states with respect to the gas potential allows young stars to migrate to the core of the ONC; and interstellar gas

protects the discs from the radiation, allowing them to live for longer than expected.

The star formation history and primordial stellar distributions in young star-forming regions are key to understanding the effects that the environment will have over the disc populations. The star formation process results in regions of varying stellar densities, far from the spherical, idealized initial conditions commonly used in models. The collapse of the giant molecular clouds (GMCs) from which stars form is shaped by turbulent flows (Falgarone et al., 1991; Falgarone & Phillips, 1991) which result in filamentary, clumpy, and fractal gas substructure in the cloud (e.g. Scalo, 1990; Larson, 1995; Elmegreen et al., 2000; Hacar et al., 2018). The mass of these clumps ranges from around one solar mass to several thousand solar masses, and sizes from less than half a parsec to tens of parsecs (e.g. Lada & Lada, 2003; Williams et al., 2000). They can form individual stars, small multiple systems, or bigger associations and clusters. The initial distribution of the stars will be a direct result of the local densities of the gas in the molecular cloud. Given that circumstellar discs emerge during the protostellar phase (Williams & Cieza, 2011), the star formation process will define the environment in which the discs are immersed in their early stages.

To get a broader understanding of the environmental effects on circumstellar discs, it is important to take a step back in time and study how the star formation process influences stellar densities. In this work we present a model for circumstellar discs inside young star forming regions. We adopt a relatively simple model for the star formation process, starting from the collapse of a giant molecular cloud to obtain masses, positions, and velocities of newly formed stars. These form the input for our star cluster evolution code. During the evolution we take into account the viscous evolution of the discs, dynamical truncations, external and internal photoevaporation, and dust evolution. We evolve the discs simultaneously with the stellar dynamics and stellar evolution.

## 2 Model

We model several different astrophysical processes which operate simultaneously and at very distinct scales: the collapse of a molecular cloud, star formation, stellar dynamics, and viscous circumstellar discs which are affected by dynamical truncations and photoevaporation. We bring these processes together using the Astrophysical Multipurpose Software Environment, AMUSE (Portegies Zwart et al., 2013; Pelupessy et al., 2013). The results presented in this work are obtained through two different simulation stages: first, we perform a simple model of the collapse of a molecular cloud and the subsequent star formation process. This returns a spatial, velocity, and mass distribution of stars to be used in the second simulation stage, in which we follow the evolution of the circumstellar discs in the star forming regions. This second stage encompasses the stellar dynamics, stellar evolution, viscous evolution of the discs, and photoevaporation. All the code developed for this work, including simulation scripts, data analyses, and figure creation is available online <sup>1</sup>.

### 2.1 Molecular cloud collapse and star formation

The first stage of the simulations deals with a simple model of the star formation process. We simulate the collapse of a molecular cloud using the smoothed particle hydrodynamics (SPH) code **Fi** (Pelupessy et al., 2004). We model the star formation process through the use of sink particles, which are created from regions of the cloud where the local gas density is higher than a threshold. We set this threshold at  $1M_{\odot}/\epsilon^3$ , where  $\epsilon = 0.05$  pc is the softening of the simulation. Once a sink particle forms it continues accreting gas from the molecular cloud. Each of these sink particles can form several stars.

Since we look to preserve a power-law mass function similar to the one observed in the galaxy, the stars in our simulations cannot be born with random masses. As a consequence, we have to introduce a predetermined star formation efficiency (SFE). We set a SFE of 0.3 (Lada & Lada, 2003). We implement this SFE by keeping track of the mass in sinks, since this is the mass that will eventually be turned into stars. When the total sinks mass reaches 30% of the mass of the cloud, the SPH code is stopped. We keep track of the existing sinks in a separate dynamics code to guarantee that they continue to move after the SPH code is stopped. The star formation process continues until all the mass in the sinks has turned into stars.

---

<sup>1</sup><https://github.com/franciscaconcha/molecular-cloud>

The star formation process begins once sink particles have accreted enough mass to sample stars from a random initial mass function (IMF). We base the star formation mechanism on Wall et al. (2019). We begin by sampling a random stellar mass  $m$  from a Kroupa IMF (Kroupa, 2001) of 10,000 stars, with lower limit  $0.08 M_\odot$  and upper limit  $150 M_\odot$  (Wall et al., 2019). Then we check if there is a sink massive enough to form a star of mass  $m$ . If there is one, we subtract the mass  $m$  from the sink and create a star particle. If  $m \leq 1.9 M_\odot$  the star will have a circumstellar disc (see section 2.2.2), and we subtract the mass of the star and the initial mass of the disc from the sink. The position of the newly formed star is determined by taking the position of the sink and adding a random offset in each spatial dimension. This offset is calculated within the sink diameter. The velocity of the new star is set to the velocity of its birth sink.

After a sink has formed a star, we set a delay time which must pass before it creates a new star. We implement this step to counteract the fact that our sampling will be biased toward forming low mass stars, by allowing sinks to become more massive before forming another star. This delay is implemented as an exponentially decaying timescale:

$$t_{\text{delay}} = t_{\text{ff}} \exp\left(\frac{-0.1 t}{1 \text{ Myr}}\right) \quad (1)$$

where  $t_{\text{ff}}$  is the free-fall time scale of the corresponding sink and  $t$  is the current model time.

During the molecular cloud collapse simulation we keep track of the mass, position, velocity, and birth time of the newly formed stars. This data will then be given as input for the second part of the simulations, which involve the disc evolution and stellar dynamics.

## 2.2 Stellar dynamics and circumstellar discs

The second simulation stage begins at the time when the first star has formed. For each star, we evolve its disc and calculate its external photoevaporation mass loss rate as explained in sections 2.2.1 and 2.2.2, respectively. The star formation process ends when all the mass in sinks has been formed into stars. Then, the leftover gas is expelled and we only deal with the stellar dynamics and processes explained in the following sections. This second stage of the simulations evolve for 2 Myr after the last star has formed. Below we describe how each of the processes is modeled.

### 2.2.1 Circumstellar discs

We model circumstellar discs using the Viscous Accretion disc Evolution Resource (VADER, Krumholz & Forbes, 2015). VADER models the viscous transport of mass and angular momentum on a thin, axisymmetric disc. We use the standard disc profile of Lynden-Bell & Pringle (1974) to establish the initial column density of the discs as:

$$\Sigma(r, t = 0) \approx \frac{m_d}{2\pi r_d (1 - e^{-1})} \frac{\exp(-r/r_d)}{r} \quad (2)$$

where  $r_d$  is the initial disc radius,  $m_d$  is the initial disc mass, and  $\Sigma_0$  is a normalisation constant. We consider the characteristic radius to be  $r_c \approx r_d$  (Anderson et al., 2013).

For the external photoevaporation process we keep track of the disc edge. We define the disc radius as the location of the disc cell closest to a density value  $\Sigma_{\text{edge}}$  (Clarke, 2007; Haworth et al., 2018a). The mass loss due to external photoevaporation (section 2.2.2), as well as dynamical truncations (section 2.2.5), causes the disc to develop a steep density profile at the outer edge. The location of the edge is insensitive to the value of  $\Sigma_{\text{edge}}$ , given that it is sufficiently low (Clarke, 2007). We set the column density outside  $r_d$  to a negligible value  $\Sigma_{\text{edge}} = 10^{-12} \text{ g cm}^{-2}$ .

Each of the VADER discs in the simulations consists of a grid of 100 logarithmically spaced cells, ranging from 0.05 au to 2000 au. All the discs have a constant turbulence parameter of  $\alpha = 5 \times 10^{-3}$ .

### 2.2.2 External photoevaporation

We calculate the mass loss due to external photoevaporation using the Far-ultraviolet Radiation Induced Evaporation of Discs (FRIED) grid (Haworth et al., 2018b). This grid provides a pre-calculated set of mass

loss rates for discs immersed in UV radiation fields of varying strengths, from  $10\text{ G}_0$  to  $10^4\text{ G}_0$ , where  $G_0$  is the FUV field measured in Habing units,  $1.6 \times 10^{-3}\text{ s}^{-1}\text{ cm}^{-2}$  (Habing, 1968). The grid spans discs of mass  $\sim 10^{-4}\text{ M}_{\text{Jup}}$  to  $10^2\text{ M}_{\text{Jup}}$ , radius from 1 au to 400 au, and host star mass from  $0.05\text{ M}_{\odot}$  to  $1.9\text{ M}_{\odot}$ .

To stay inside the boundaries of the FRIED grid we consider only stars of mass  $M_* \leq 1.9\text{ M}_{\odot}$  as having a circumstellar disc. More massive stars are considered to generate radiation. This mass distinction is for external photoevaporation calculations only; for the stellar dynamics evolution there is no separation between these two stellar groups.

Far-ultraviolet (FUV) photons dominate in the external photoevaporation process (Armitage, 2000; Adams et al., 2004; Gorti & Hollenbach, 2009). We calculate the FUV radiation from the massive stars by pre-computing a relation between stellar mass and FUV luminosity using the UVBLUE spectral library (Rodríguez-Merino et al., 2005). The obtained fit is presented in Figure 2 of Concha-Ramírez et al. (2019b). We use that fit to determine the FUV radiation emitted by each massive star at every simulation time step.

We model the external photoevaporation process as follows. At every time step we calculate the distance from every disc to every star of mass  $M_* > 1.9\text{ M}_{\odot}$  and determine the total radiation received by each disc. We do not consider extinction due to interstellar material. We interpolate from the FRIED grid using the calculated total radiation and the disc parameters to find a photoevaporation driven mass loss rate for each disc. Assuming the mass loss rate  $\dot{M}$  to be constant during the current time step, we use it to calculate the total mass loss. This mass is then removed from the outer regions of the disc. We move through the disc cells starting from the outermost one, removing mass from each, until the required amount of mass has been removed. External photoevaporation then results in a decrease of disc mass and disc radius.

Under certain circumstances, external photoevaporation can be dominated by extreme ultraviolet (EUV) photons. This happens when a disc is closer to a radiating star than a minimum distance derived by Johnstone et al. (1998) as:

$$d_{min} \simeq 5 \times 10^{17} \left( \frac{\varepsilon^2}{f_r \Phi_{49}} \right)^{-1/2} r_{d14}^{1/2} \text{ cm} \quad (3)$$

where  $f_r$  is the fraction of EUV photons absorbed in the ionizing flow,  $\Phi_{49} = \frac{\Phi_i}{10^{49}\text{ s}^{-1}}$  is the EUV luminosity of the source,  $\varepsilon$  is a dimensionless normalizing parameter,  $\left( \frac{\varepsilon^2}{f_r \Phi_{49}} \right)^{1/2} \approx 4$ , and  $r_{d14} = \frac{r_d}{10^{14}\text{ cm}}$  with  $r_d$  the disc radius.

When the distance  $d$  between a disc and a massive star is  $d < d_{min}$ , the disc enters the EUV-dominated photoevaporation regime. The mass loss in this case is calculated as:

$$\dot{M}_{EUV} = 2.0 \times 10^{-9} \frac{(1+x)^2}{x} \varepsilon r_{d14} \text{ M}_{\odot} \text{ yr}^{-1} \quad (4)$$

with  $x \approx 1.5$  and  $\varepsilon \approx 3$  (Johnstone et al., 1998).

A disc is dispersed when it has lost 99% of its initial mass (Anderson et al., 2013) or when its mean column density drops below  $1\text{ g/cm}^2$  (Pascucci et al., 2016). After a disc is dispersed, its host star continues to evolve normally in the stellar dynamics code.

### 2.2.3 Internal photoevaporation

Internal photoevaporation is driven by X-ray radiation (Owen et al., 2010, 2012). We calculate the X-ray luminosity of the stars with discs using the fit obtained by Flaccomio et al. (2012) for T-Tauri stars as a function of stellar mass:

$$\log(L_X) = 1.7 \log \left( \frac{M_*}{1\text{ M}_{\odot}} \right) + 30 \text{ erg s}^{-1} \quad (5)$$

where  $M_*$  is the mass of the host star.

Picogna et al. (2019) calculate X-ray mass loss profiles and mass loss rates for a star of mass  $0.7\text{ M}_{\odot}$ . Owen et al. (2012) developed scaling relations that allow to calculate these values for stars with masses  $M_* \leq 1.5\text{ M}_{\odot}$ . We combine the results of Picogna et al. (2019) with the scaling relations of Owen et al.

(2012) to span a larger range of stellar masses. The internal photoevaporation mass loss rate is then given by:

$$\dot{M}_X = 10^\Delta \left( \frac{M_*}{0.7 M_\odot} \right)^{-0.068} M_\odot \text{ yr}^{-1}, \quad (6)$$

where

$$\Delta = -2.7326 \exp \left[ \frac{(\ln(\log(L_X)) - 3.3307)^2}{2.9868 \times 10^{-3}} \right] - 7.2580 \quad (7)$$

is the X-ray mass loss rate derived by Picogna et al. (2019).

The mass loss profile takes the form:

$$\begin{aligned} \dot{\Sigma}_w(x) = \ln(10) \left( \frac{6a \ln(x)^5}{x \ln(10)^b} + \frac{5b \ln(x)^4}{x \ln(10)^5} + \frac{4c \ln(x)^3}{x \ln(10)^4} + \frac{3d \ln(x)^2}{x \ln(10)^3} \right. \\ \left. + \frac{2e \ln(x)}{x \ln(10)^2} + \frac{f}{x \ln(10)} \right) \frac{\dot{M}_w}{2\pi x} M_\odot \text{ au}^{-2} \text{ yr}^{-1}, \quad (8) \end{aligned}$$

where

$$\dot{M}_w(x) = \dot{M}_X 10^{a \log x^6 + b \log x^5 + c \log x^4 + d \log x^3 + e \log x^2 + f \log x + g} \quad (9)$$

with  $a = -0.5885$ ,  $b = 4.3130$ ,  $c = -12.1214$ ,  $d = 16.3587$ ,  $e = -11.4721$ ,  $f = 5.7248$ , and  $g = -2.8562$  (Picogna et al., 2019); and

$$x = 0.85 \left( \frac{r}{\text{au}} \right) \left( \frac{M_*}{1 M_\odot} \right)^{-1} \quad (10)$$

is the scaling from Owen et al. (2012), where  $M_*$  is the mass of the host star.

The internal photoevaporation process removes mass from the disc following the profile defined in Eq. 8. In the case where a grid cell contains less mass than is prescribed to be removed, this excess is removed in the nearest outer cell. As the cells are traversed inside-out, this takes the form of inside-out disc clearing.

## 2.2.4 Disc dust evolution

Circumstellar discs are composed of gas and dust. In general, a 100:1 gas:dust ratio is assumed for the composition of the discs. This value is derived from the consideration that the ratio is inherited from the interstellar medium (Bohlin et al., 1978). Grain growth might result in much lower gas:dust ratios (Williams & Best, 2014), and the ratio is likely to change during the lifetime of a disc (Manara et al., 2020). Models of dust evolution and radial drift (Birnstiel et al., 2010; Rosotti et al., 2019) show that the dust:gas ratio decreases in time. In the present work we introduce a simple prescription for the dust evolution inside circumstellar discs.

We follow the prescription of Haworth et al. (2018a) to calculate the mass loss rate of dust entrapped in the photoevaporation wind. This mass loss rate is described as:

$$\dot{M}_{dw} = \delta \dot{M}_{gas}^{3/2} \left( \frac{\nu_{th}}{4\pi F G M_* \rho_g a_{min}} \right)^{1/2} \exp \left( \frac{-\delta (GM)^{1/2} t}{2 R_d^{3/2}} \right), \quad (11)$$

where  $\delta$  is the initial dust:gas ratio ( $10^{-2}$ ),  $\dot{M}_{gas}$  is the gas mass loss rate (determined as explained in sections 2.2.2 and 2.2.3),  $\nu_{th} = \sqrt{8k_b T / \pi \mu / m_H}$  is the mean thermal speed of the gas particles,  $F$  is the solid angle subtended by the disc at the outer edge,  $\rho_g$  is the grain mass density ( $1 \text{ g/cm}^3$ , Facchini et al. (2016)), and  $a_{min}$  is the minimum grain size at the disc radius  $R_d$ . We assume  $a_{min} = 0.01 \mu\text{m}$  (Haworth et al., 2018a; Facchini et al., 2016).

This model takes into account what fraction of the dust is entrained in the photoevaporation wind, and how it decreases over time due to dust growth. Mass is removed from a single, scalar reservoir. The radial structure is implicitly assumed to follow the gas structure, multiplied by the dust-to-gas ratio  $\delta \sim 0.01$ , and doesn't account for the dust fraction enhancement due to the evaporation-resistant dust population.

### 2.2.5 Dynamical truncations

We calculate a semi-analytical truncation radius based on Adams (2010), who propose that the new radius of a disc after a truncating encounter is  $R' \approx b/3$  where  $b$  is the pericentre distance of the encounter. We combine this with the mass dependence of Breslau et al. (2014) to define a truncation radius:

$$R' = \frac{r_{enc}}{3} \left( \frac{m_1}{m_2} \right)^{0.32}, \quad (12)$$

where  $m_1$  and  $m_2$  are the masses of the encountering stars. We follow (Portegies Zwart, 2016) in defining an initial collisional radius of  $r_{col} = 0.02$  pc for all stars. This value is updated to  $r_{col} = 0.5r_{enc}$  after every encounter, to make sure that each encounter is only detected once within the time step. Not all encounters result in disc truncation. If the calculated truncation radius  $R'$  is larger than the current radius of an encountering disc, the disc is not affected by the encounter. If a disc is truncated in an encounter, we set the new radius of a disc to  $R'$  by making the column density  $\Sigma_{edge} = 10^{-12} \text{ g cm}^{-2}$  for every disc cell outside  $R'$ . The truncated disc then continues to expand viscously.

Dynamical encounters not only change the disc sizes and strip mass from the outskirts, but can also lead to changes in the mass distribution of the discs and mass exchange can occur between the encountering discs (Pfalzner et al., 2005b; Rosotti et al., 2014; Jílková et al., 2015; Portegies Zwart, 2016). Because of our implementation of the discs (section 2.2.1) we do not consider mass exchange or any other changes to the mass distribution during dynamical encounters, other than truncation. When a disc is truncated in our model, all the mass outside its new radius  $R'$  is simply lost.

## 2.3 Initial conditions

### 2.3.1 Molecular cloud

Our simulations start with an spherical cloud model of mass  $10^4 M_\odot$  and initial radius 3 pc. We use 32,000 SPH particles, which results in a resolution of  $0.3 M_\odot$  per particle. The softening in the simulations is 0.05 pc. Each realization of a molecular cloud has a different random seed, so the substructure that originates is different in every run of the simulation. We run 6 realizations of the molecular cloud collapse simulations, which differ only in the random seed.

### 2.3.2 Circumstellar discs

We define the initial disc radii as:

$$r_d(t=0) = R' \left( \frac{M_*}{M_\odot} \right)^{0.5}, \quad (13)$$

where  $R'$  is a constant. We choose  $R' = 30 \text{ au}$ , which results in initial disc radii between  $\sim 5 \text{ au}$  and  $\sim 40 \text{ au}$ . This is in agreement with observations that suggest that young circumstellar discs are generally quite compact (radii around 20 to 50 au, (Trapman et al., 2020; Tobin et al., 2020)). We set the initial radius of each disc on the grid through the procedure explained in section 2.2.1.

The initial mass of the discs is defined as:

$$M_d(t=0) = 0.1 M_*. \quad (14)$$

This yields initial disc masses ranging from  $\sim 8 M_{Jup}$  to  $\sim 200 M_{Jup}$ .

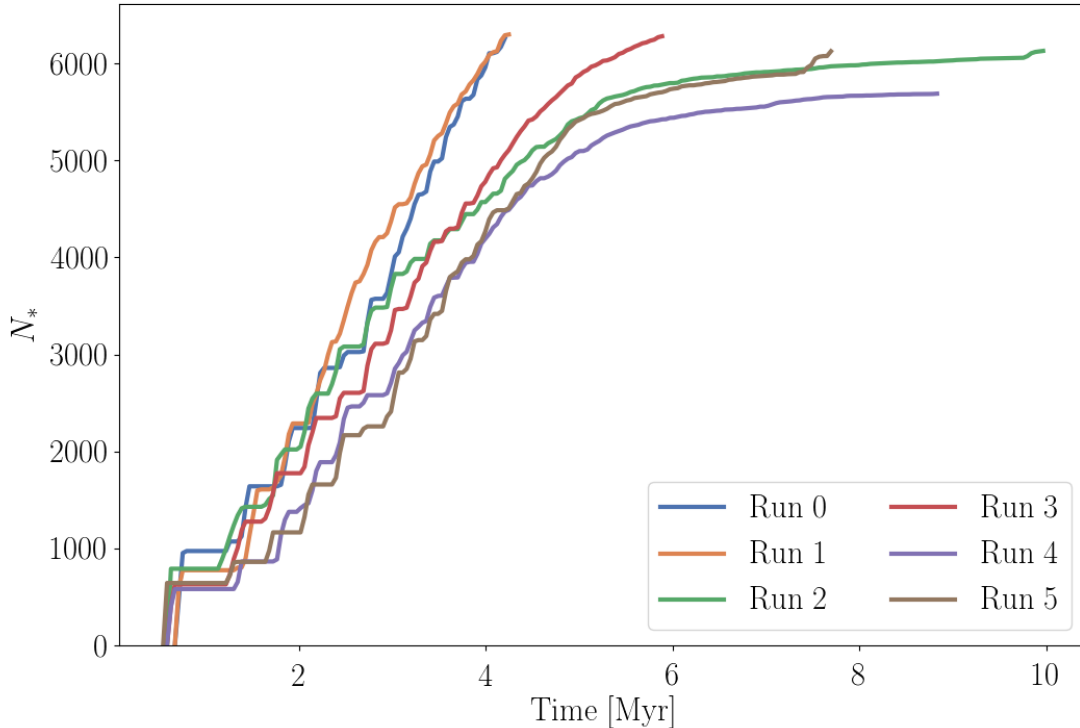


Figure 1: Number of stars in time for each simulation run.

### 3 Results

#### 3.1 Star formation and cluster evolution

In Figure 1 we show the number of stars in time for each simulation run. In Table 1 we present the final number of stars in each run. The mean number of stars created in six runs is  $6146 \pm 214$ .

To quantify the spatial distribution of the stars resulting from the molecular cloud collapse simulations, we look at the  $Q$  parameter of the minimum spanning tree (Cartwright & Whitworth, 2004) and the fractal dimension in each region at the end of the star formation process. The  $Q$  parameter is calculated as:

$$Q = \frac{\overline{m}}{\overline{s}}, \quad (15)$$

where  $\overline{m}$  is the mean length of the minimum spanning tree and  $\overline{s}$  is the mean separation between the stars. Regions with  $Q > 0.8$  are smooth and centrally concentrated, while values of  $Q < 0.8$  correspond to regions with substructure.

In Figure 2 we show the  $Q$  parameter versus age for each of our simulations, along with values for several observed regions. In the case of the simulations, the ages used in this plot correspond to the moment when star formation ends. The  $Q$  parameter of the simulations is calculated from a 2D projection of the stellar distances. In Table 2 we summarize the values for  $Q$  and the estimated ages for each region, along with the corresponding references. The simulation results span a range of  $Q \sim 0.6$  to  $Q \sim 0.8$ , which means that some substructure is still present. Regions with lower  $Q$ , such as Corona Australis (Parker, 2014), Cygnus OB2 (Wright et al., 2014), and Taurus (Cartwright & Whitworth, 2004) are highly substructured. In observations of star forming regions,  $Q$  might vary depending on membership uncertainty (Parker & Meyer, 2012). This



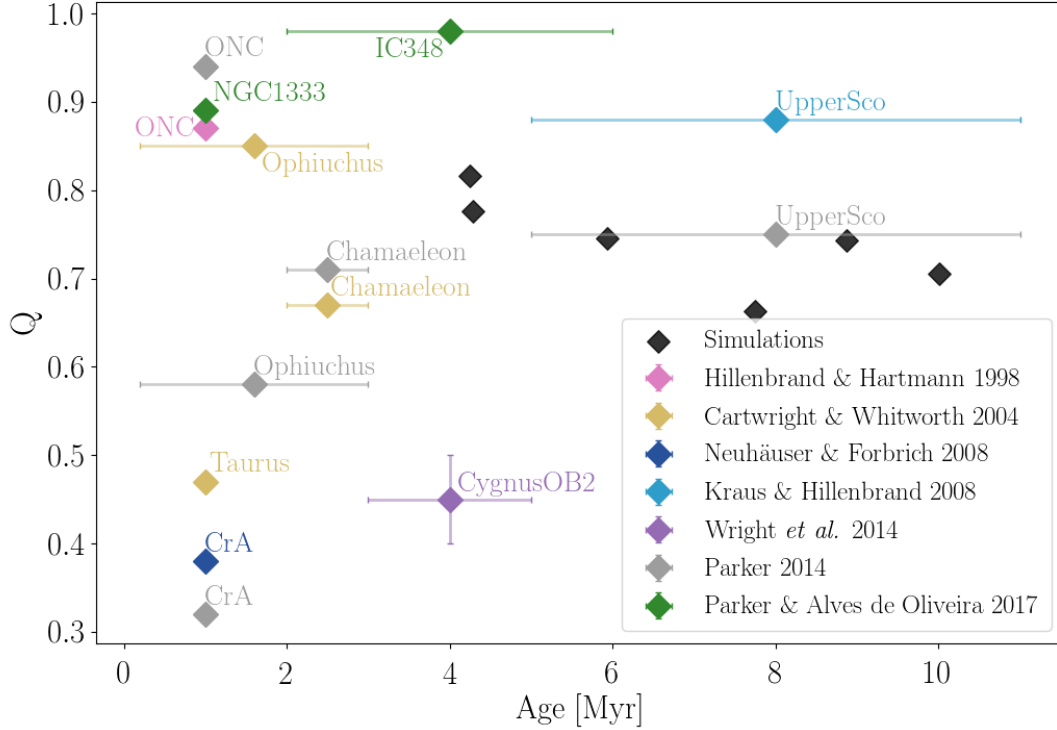


Figure 2: Q parameter of our simulations and observed star forming regions. The ages at which the simulation points are plotted correspond to the moment in the simulation when star formation ends.

leads to some regions having more than one value of  $Q$ , such as Corona Australis, Chamaeleon, the ONC, Ophiuchus, and Upper Scorpio.

Another way to quantify the structure of a star forming region is by measuring its fractal dimension,  $F_d$ . In Figure 3 we show the evolution of the fractal dimension in time for each simulation run, along with a Plummer sphere of 6000 stars and initial virial radius 3 pc for comparison. The solid lines show the fractal dimension while star formation is still ongoing. The dotted lines show the evolution after the star formation process has ended. Once a region reaches a stable value of  $F_d$ , it remains the same up to the end of the simulation. We also show measured values of the fractal dimension for several observed regions. As with the  $Q$  parameter, when measuring the fractal dimension from observations the values might vary depending on membership, leading to regions with more than one value of  $F_d$ . In Table 2 we present the values of  $F_d$  for all observed regions.

In Figure 4 we show the evolution of the virial radius in time for each of our simulations. We also show the virial radius as a function of time of a Plummer sphere with 6000 stars and initial virial radius 3 pc for comparison. The solid lines show the virial radius while star formation is still ongoing, whereas the dotted lines follow the radius after all stars have formed and gas has been removed from the clusters. It can be seen that all the regions expand quickly after the gas is expelled.

### 3.2 Disc masses

In Figure 5 we show the disc mass versus local number density for all simulation runs. The left panel shows the discs at the end of the star formation process. The right panel shows the discs at the end of the simulations, 2 Myr after star formation has finished. The color of each disc represents the time at which

Table 1: Run number, final number of stars ( $N_*$ ), time of the end of star formation ( $t_{\text{end}}^{\text{SF}}$ ), Q parameter, and fractal dimension ( $F_d$ ) for our simulation results.

Region	$N_*$	$t_{\text{end}}^{\text{SF}}$ [Myr]	Q	$F_d$
Run #1	6289	4.25	0.816	1.6
Run #2	6315	4.29	0.776	1.5
Run #3	6162	10.01	0.705	1.7
Run #4	6283	5.93	0.745	1.5
Run #5	5691	8.87	0.743	1.4
Run #6	6137	7.74	0.663	1.6

Table 2: Region name, number of stars ( $N_*$ ), age, Q parameter, and fractal dimension ( $F_d$ ) for our simulation results and observed regions. References: (a) Parker (2014); (b) Neuhäuser & Forbrich (2008); (c) Luhman et al. (2016); (d) Parker & Alves de Oliveira (2017); (e) Hillenbrand & Hartmann (1998); (f) Cartwright & Whitworth (2004); (g) Hartmann (2002); (h) Kraus & Hillenbrand (2008); (i) Simon (1997); (j) Bontemps et al. (2001); (k) Luhman (2007); (l) Wright et al. (2010); (m) Wright et al. (2014); (n) Carpenter et al. (2006); (o) Luhman & Mamajek (2012); (p) Sacco et al. (2017); (q) Galli et al. (2020); (r) Luhman & Esplin (2020); (s) Luhman (2018).

Region	$N_*$	Age [Myr]	Q	$F_d$
Corona Australis (CrA)	$\sim 313^{(q)}$	$\sim 1.0^{(a)}$	$0.32^{(b)}$ , $0.38^{(a)}$	-
NGC 1333	$\sim 200^{(e)}$	$\sim 1.0^{(c)}$	$0.89^{(d)}$	-
ONC	$\sim 1000^{(e)}$	$\sim 1.0^{(e)}$	$0.87^{(e)}$ , $0.94^{(a)}$	-
Taurus	$\sim 438^{(s)}$	$\sim 1.0^{(f)}$	$0.47^{(f)}$	$1.5^{(f)}$ , $1.02 \pm 0.04^{(g)}$ , $1.049 \pm 0.007^{(h)}$ , $1.5 \pm 0.2^{(i)}$
Trapezium	$\sim 1000^{(e)}$	$\sim 1.0^{(e)}$	-	$1.5 \pm 0.2^{(i)}$
Ophiuchus	$199^{(f)}$	$1.6 \pm 1.4^{(j)}$	$0.85^{(f)}$ , $0.58^{(a)}$	$1.5 \pm 0.2^{(i)}$
Chamaeleon I	$120^{(p)}$	$2.5 \pm 0.5^{(k)}$	$0.67^{(f)}$ , $0.71^{(a)}$ , $0.80 \pm 0.08^{(p)}$	$2.25^{(f)}$
Cygnus OB2	$\sim 2700^{(l)}$	$4.0 \pm 1.0^{(l)}$	$0.45 \pm 0.05^{(m)}$	-
IC 348	$\sim 500^{(c)}$	$4.0 \pm 2.0^{(c)}$	$0.98^{(d)}$	-
Upper Scorpio	$\sim 1761^{(r)}$	$8.0 \pm 3.0^{(n)}$	$0.88^{(h)}$ , $0.75^{(a)}$	$0.69 \pm 0.09^{(h)}$

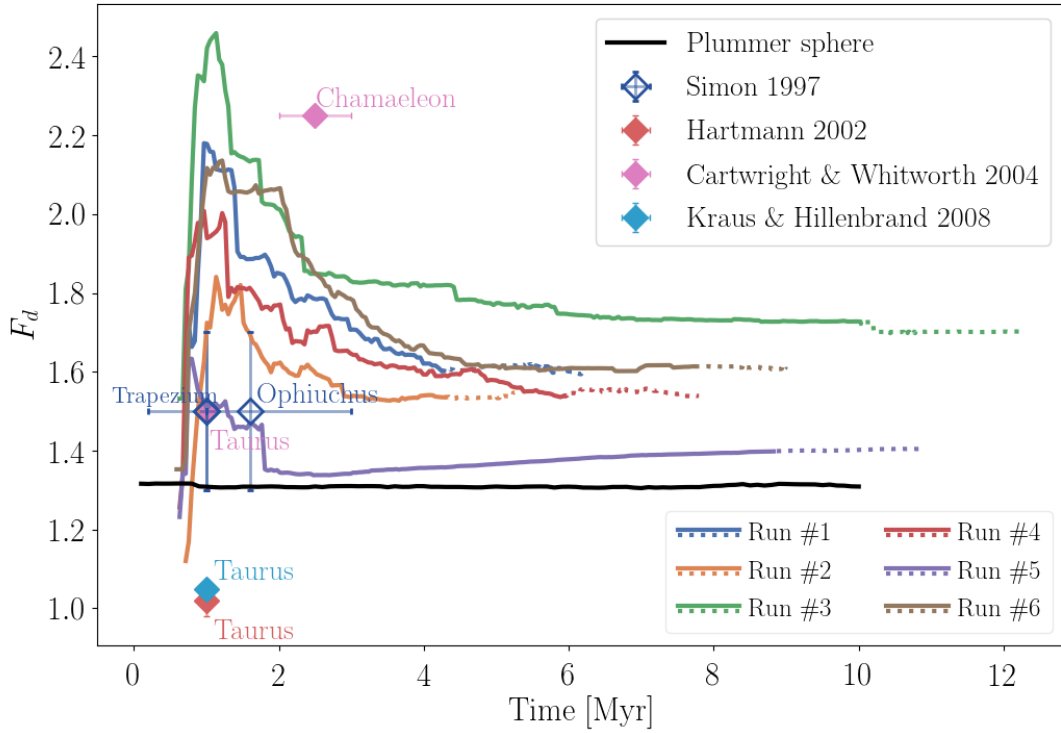


Figure 3: Fractal dimension of the simulations in time. The solid lines correspond to the fractal dimension while star formation is still ongoing, and the dotted lines after it has ended. The black line shows the fractal dimension in time of a Plummer sphere with 6000 stars and initial virial radius 3 pc for comparison.

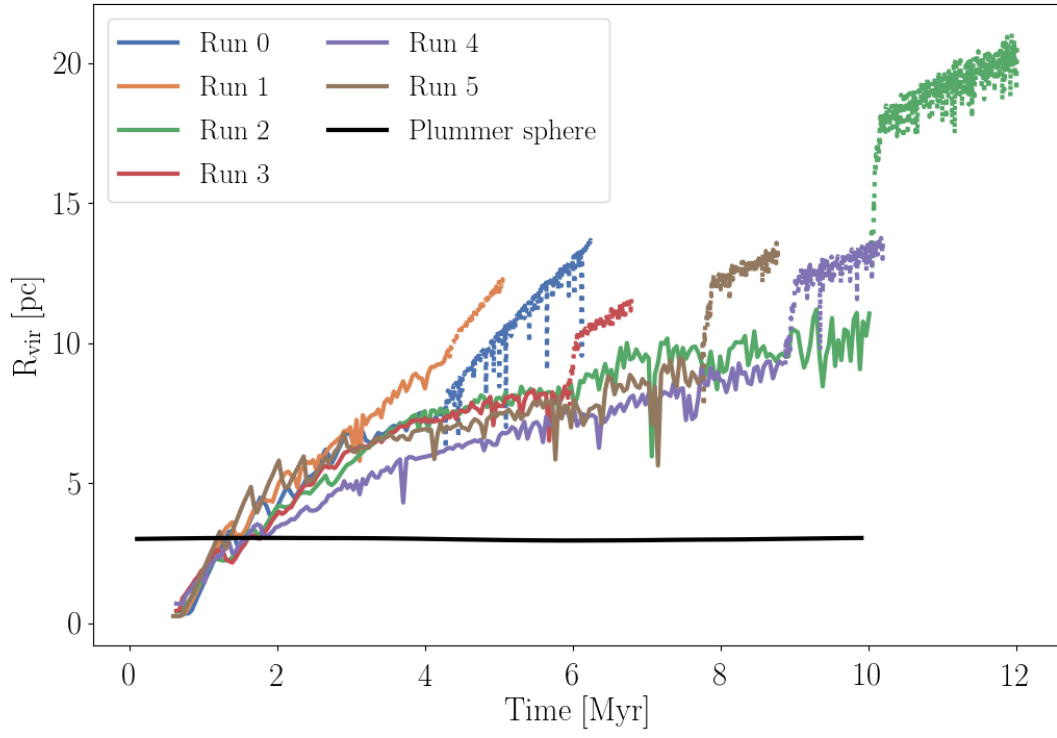


Figure 4: Virial radius of the simulations in time. The solid lines correspond to the virial radius while star formation is still ongoing, and the dotted lines after it has ended. The black line shows the virial radius in time of a Plummer sphere with 6000 stars and initial virial radius 3 pc for comparison.

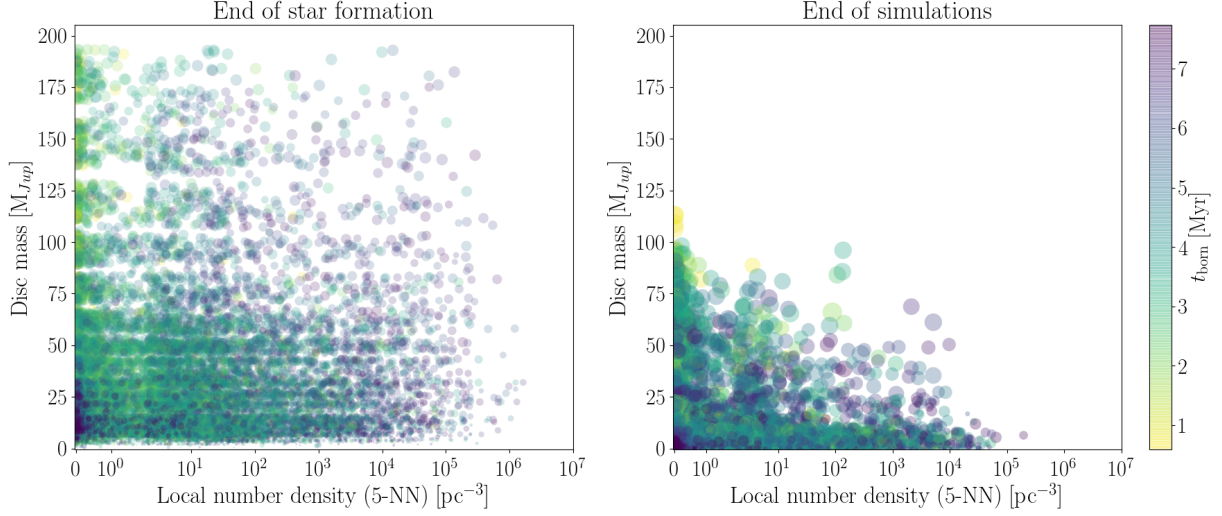


Figure 5: Disc mass versus local number density for all discs in all simulation runs. The left panel shows the discs at the end of the star formation process. The right panel shows the discs at the end of the simulations, 2 Myr after star formation has finished. The size of the points is proportional to the disc radius. The color shows the time at which each disc was born.

it was born. We calculate the local stellar density using the method by Casertano & Hut (1985) with the five nearest neighbours. While star formation is still ongoing, stars and discs form in regions spanning the whole range of stellar density. In particular, given our implementation of the star formation process with sink particles, many stars tend to form in regions of high stellar densities. Once the star formation process ends and the gas is expelled, the clusters expand to regain virial equilibrium. This brings an overall decrease in local number density. As stars are no longer being formed, the areas of high stellar density become less populated, since discs are losing mass due to photoevaporation. By the end of the simulations, almost no discs are present in regions of local density  $\gtrsim 10^5$  stars  $\text{pc}^{-3}$ . Even in low density regions, the maximum disc mass decreases from  $\sim 200 M_{Jup}$  to  $\sim 150 M_{Jup}$ . Massive, large discs are present only in regions of low stellar density.

In Figure 6 we show the mean dust mass in time for the discs in each run. The solid lines show the times while star formation is still ongoing, and the dotted lines once the last star has formed. While star formation is still happening, there is variability in the mean disc mass given the fact that some discs are exposed to external photoevaporation and some new discs are being formed. However, once star formation stops, the decrease in disc mass is sharp.

In Figure 7 we present the binned mean gas and dust masses of the discs versus the projected local stellar number density, at the end of the simulations. The local stellar density is calculated in the same way as for Figure 5, but with the distances between stars projected to two dimensions. The binned mean is calculated using a rolling bin spanning 100 stars. The dust mass remains relatively constant across densities, whereas the gas mass shows a slight decrease with stellar density. This can be explained by the fact that some dust is lost in photoevaporation early on, but it soon becomes resilient to this effect. Gas, on the other hand, is consistently lost throughout the simulations.

In Figure 8 we show the cumulative distribution of disc dust masses at the end of star formation and at the end of the simulations. The lines show the mean values for all runs and the shaded areas show the standard deviation. By the end of star formation, all existing discs have dust masses  $\gtrsim 50 M_{\oplus}$ , up to  $\sim 500 M_{\oplus}$ . After 2 Myr of evolution, the distribution spans discs with dust masses from  $\sim 10^{-1} M_{\oplus}$  to  $\sim 400 M_{\oplus}$ .

In Figure 9 we show the evolution of the mean dust-to-gas disc mass ratio, or  $\delta = M_{\text{dust}}/M_{\text{gas}}$  in time. By definition, the discs in the simulations are initialized with a value of  $\delta = 10^{-2}$ . As gas mass is lost from the discs due to photoevaporation, this ratio tends to increase in time. By the end of the simulations the

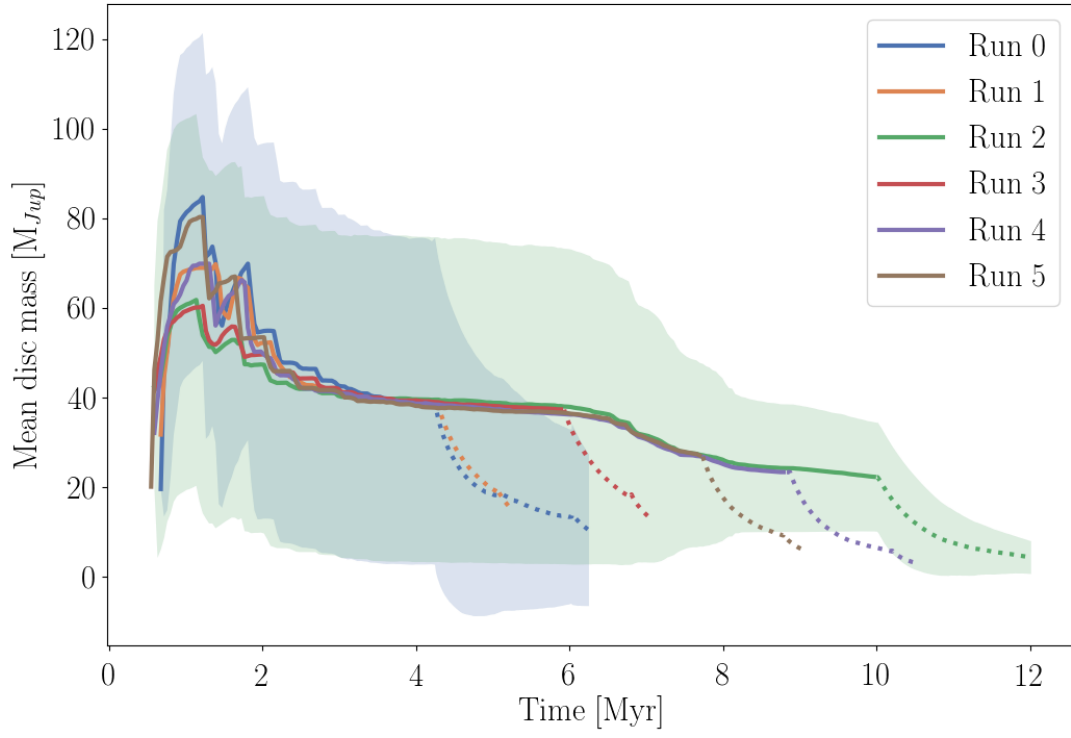
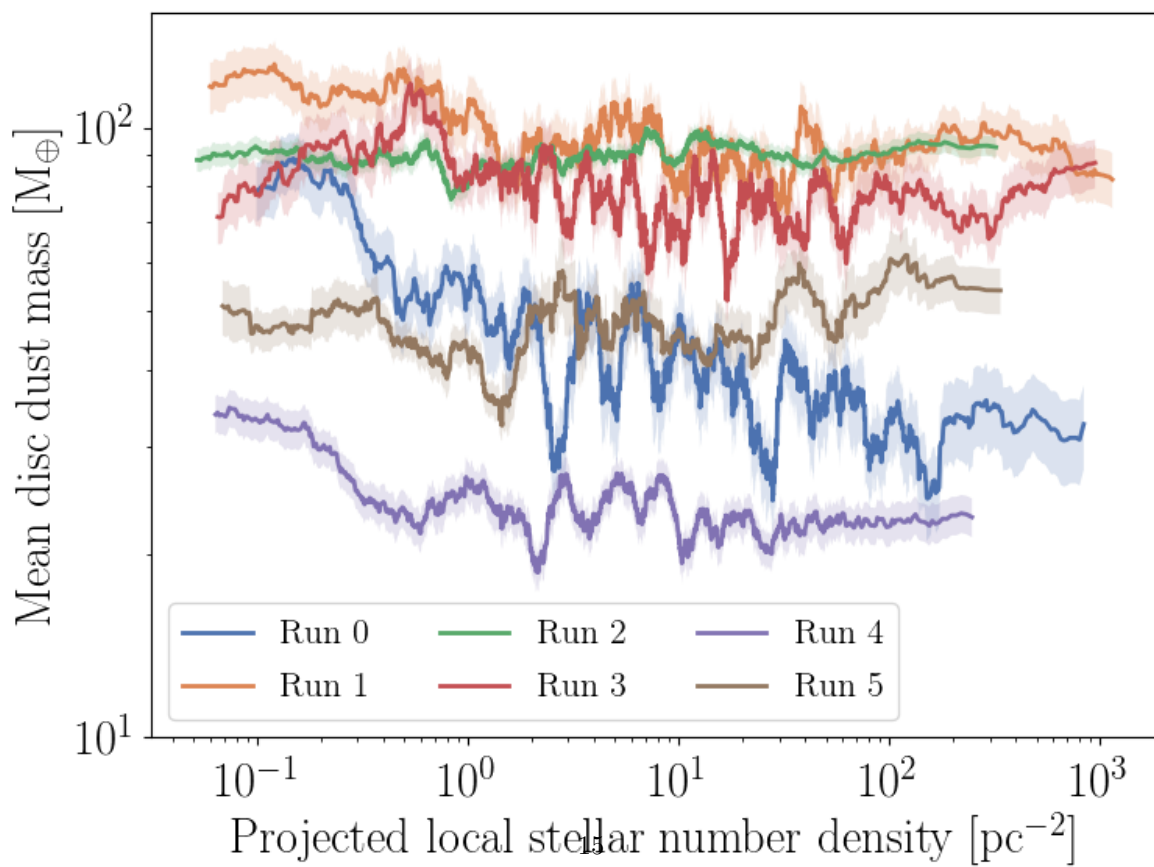
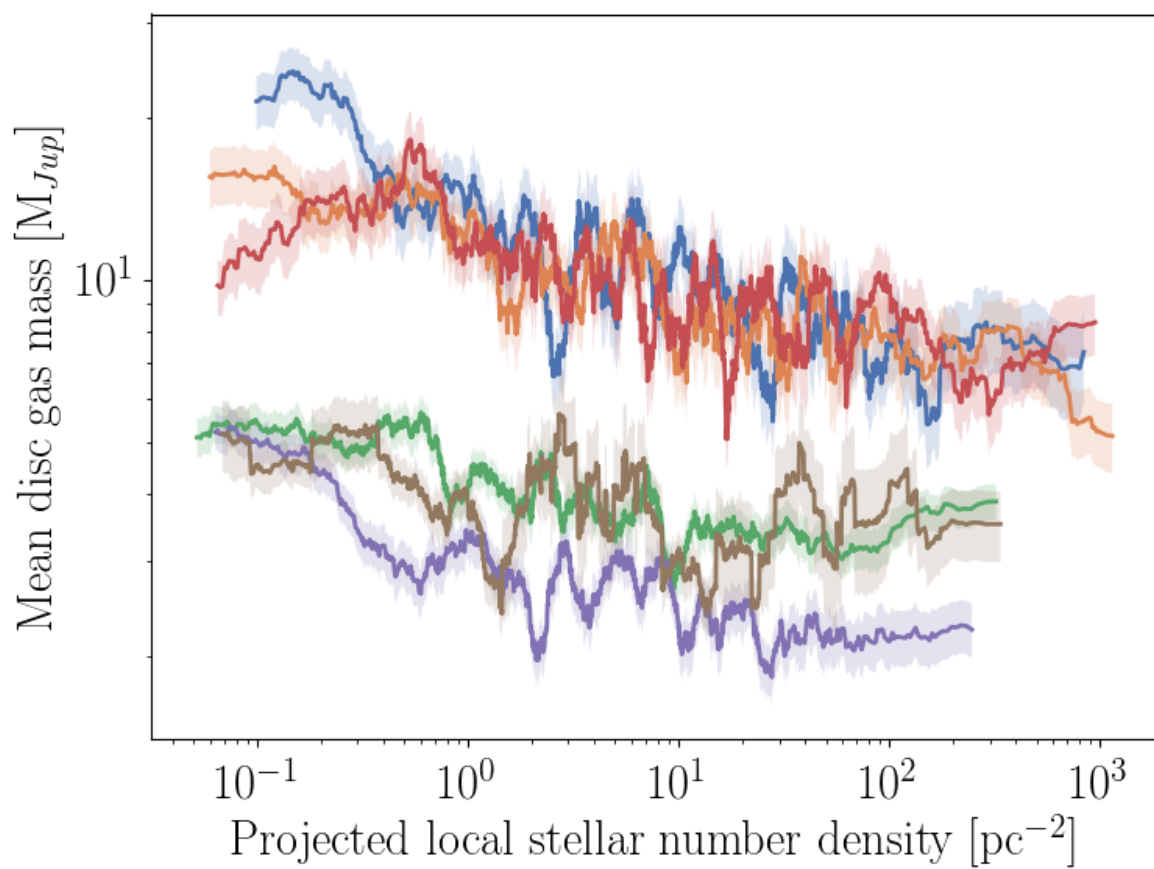


Figure 6: Mean disc dust mass in time for each simulation run. The solid lines correspond to ongoing star formation, and the dotted lines after it has ended. The standard deviation in one of the runs is shown as an example; the other runs have standard deviations of similar magnitude.



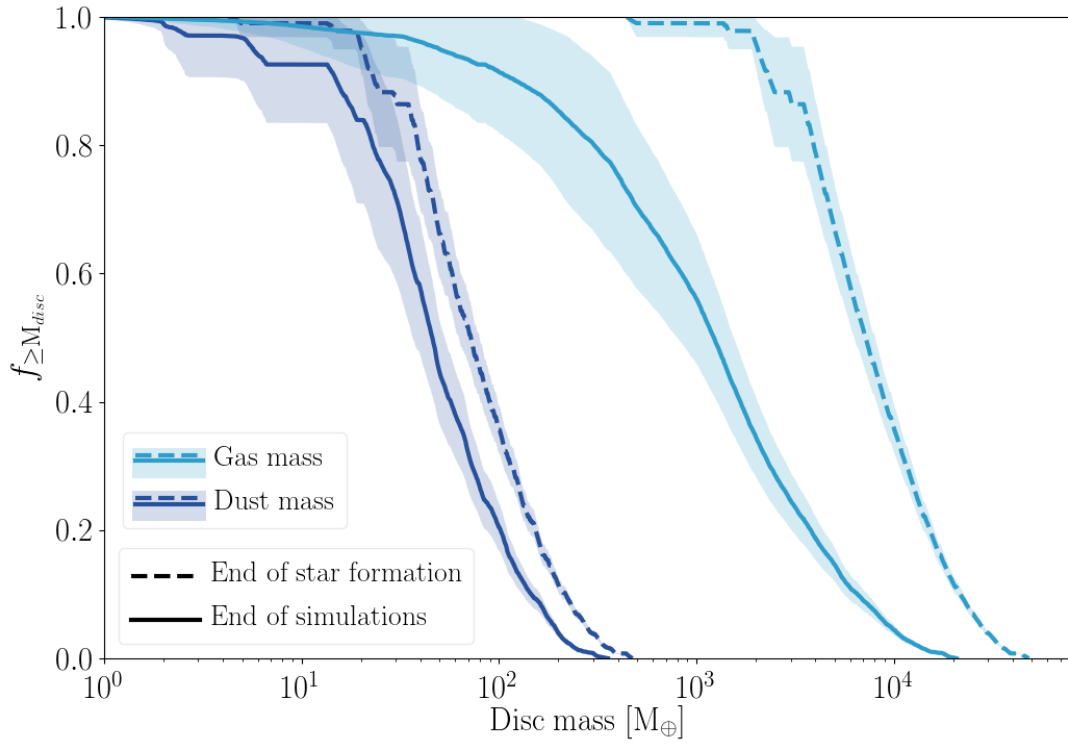


Figure 8: Cumulative distribution of disc dust and gas masses at the end of star formation (dashed lines) and at the end of the simulations (solid lines). The lines show the mean values for all runs and the shaded areas show the standard deviation.



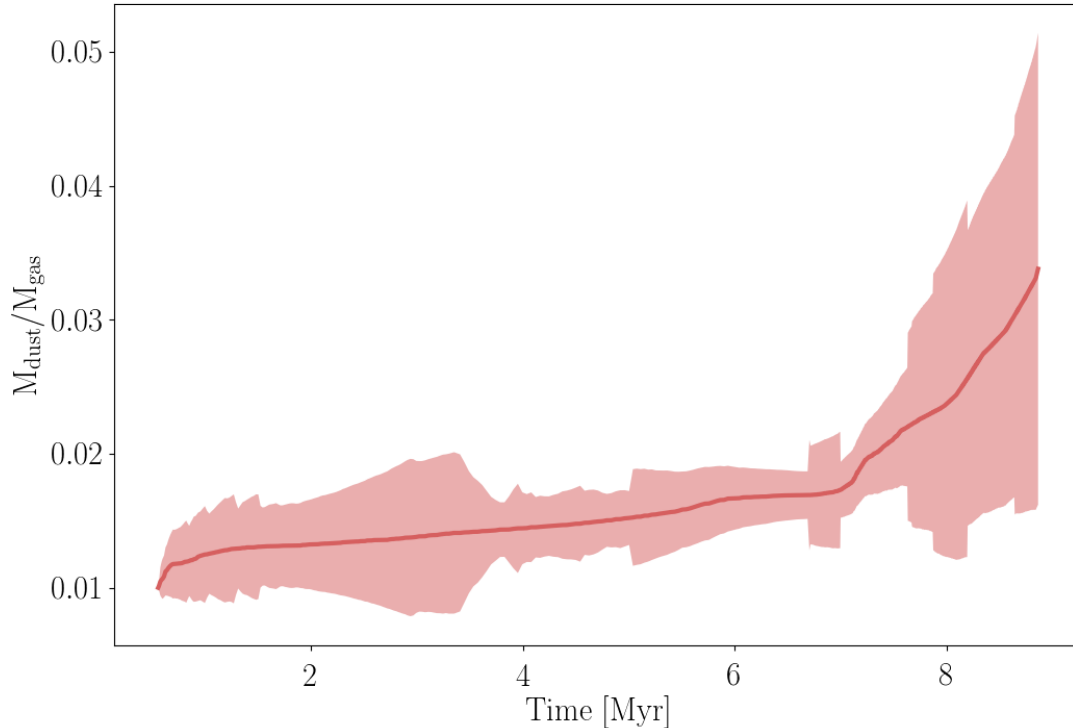


Figure 9: Mean  $M_{\text{dust}}/M_{\text{gas}}$  versus time.

mean value is  $\delta \approx 3 \times 10^{-2}$ . In some cases, particularly early on, this ratio also decreases in time due to a fraction of the dust mass being entrapped in the photoevaporation wind. The dust quickly becomes resistant to photoevaporation, but gas continues being removed from the discs.

## 4 Discussion

In previous work (Concha-Ramírez et al., 2019b, 2020) we performed simulations of star clusters where stars with masses  $M_* \leq 1.9M_{\odot}$  have circumstellar discs. These discs were subject to viscous evolution and external photoevaporation. We assumed the dust mass to be 1% of the total disc mass, and that only gas mass is removed through photoevaporation. In those previous simulations we found that discs get depleted of mass quickly enough so that  $\sim 60\%$  to  $90\%$  of them (depending on the stellar density of the region) are completely dispersed within 2 Myr of evolution. The initial spatial distribution of the stars were Plummer spheres, and all stars were formed at the same time and evolved for the full 2 Myr that the simulations lasted.

In the present work we improve our previous model in two main ways. First, we implement a simple model of molecular cloud collapse and star formation. This results in the stars not having spherical initial distributions, and in new stars being added to the simulation in time throughout an extended star formation process. Second, we implement a simple model of the dust in the discs (Haworth et al., 2018a), in order to follow its evolution directly and not simply approximate it to 1% of the total mass.

During the first few million years of evolution the star formation process is ongoing and, as discs lose mass due to photoevaporation, the new discs that are constantly being formed keep the mean mass of the overall population relatively unaffected (Figure 6). As soon as this constant replenishing of stars and discs stops, the mean mass of the discs quickly drops. This is consistent with the results from Concha-Ramírez et al. (2019b) and Concha-Ramírez et al. (2020). However, disc masses at the end of the simulations (see

Figure 7 and the bottom panel of Figure 5) are higher than in our previous simulations. In particular, unlike in our previous calculations, the dust masses in this work do not diminish as strongly with increasing stellar density.

This discrepancy can be explained by an interplay of different processes. The dust model that we implement is such that some dust is initially trapped in the photoevaporation wind. As the discs continue to evolve, the dust becomes resistant to photoevaporation and it is mostly gas mass that is lost from the discs. After a few hundred thousand years of evolution, the amount of dust mass becomes independent of the radiation received by the discs. The gas mass does decrease with increasing stellar density (see top panel of Figure 7) and in time (Figure 6). Ansdell et al. (2016) propose that a rapid depletion of gas mass in discs can lead to the observed characteristics of exoplanet populations. Traditional theories of planet formation suggest that  $\sim 10M_{\oplus}$  cores should be able to rapidly accrete gaseous envelopes, and reach masses of  $\sim 1M_{Jup}$  within  $\sim 0.1$  Myr when gas is still available in the disc. However, observational surveys show that “super-Earths”, or intermediate-mass rocky planets, are about an order of magnitude more common than gas giants (e.g. Petigura et al., 2013). Ansdell et al. (2016) suggest that, if typical  $\sim 10M_{\oplus}$  cores form in discs which are already depleted of gas, this would result in the observed discrepancy in the number of planetary types. The evolution of dust and gas disc masses in our simulations suggests a similar context for planet formation.

Another mechanism which affects our results is the long-lived star formation process. In our previous work all the stars and discs were formed at the start of the simulations and evolved for the same amount of time. In our current simulations, some discs are destroyed while new stars with discs are forming constantly. By the end of the simulations, the stars span ages from  $\sim 2$  Myr (the simulations evolve for 2 Myr after star formation has ended, so the last stars to form are slightly older than this) to  $\sim 12$  Myr, if we consider the first stars formed in our longest-running realization as the eldest ones. In Concha-Ramírez et al. (2019b) we show that around 60% of discs are destroyed by photoevaporation within the first 100,000 years of evolution in a region of stellar density  $\sim 100$  stars  $\text{pc}^{-3}$ . Similar rapid effects of photoevaporation are found in Concha-Ramírez et al. (2020). While discs are also destroyed quickly in the present simulations, the fact that discs are constantly being added to the region helps keep the disc number and disc masses higher. Massive, radiating stars also do not form all at the same time, and because of the way we implement the star formation process (see Section 2.1), they tend to form later in our simulations than low mass stars. This also gives discs more time to evolve, and the older discs will be immersed in lower radiation fields during most of their life than the younger discs.

The gas present in the clusters during the star formation process also affects the final masses of the discs in our simulations. While we do not take into account the dampening effects of the gas on radiation, the gas in our simulations does have important consequences for the dynamics of the regions. As can be seen in Figure 4, after star formation ends and the gas is expelled, the clusters quickly expand to regain virial equilibrium. This expansion leads to a decrease in the local stellar densities and an increase in the distance between stars, both which reduce the amount of radiation received by the discs.

Considering the absorption of radiation by the gas results in a protective effect for the discs, with the gas actively shielding them from external photoevaporation. The presence of gas is an important point determined by Winter et al. (2019a) to reproduce the disc population of Cygnus OB2, and to explain the so-called ‘proplyd lifetime problem’ discussed below. Observational surveys also suggest the presence of gas being protective for the discs (e.g. van Terwisga et al., 2020). Our model shows that the effects of the gas over the dynamics of the regions could also have an important effect in the final disc fractions and disc mass distributions.

The ‘proplyd lifetime problem’ is the name given to the fact that circumstellar discs are observed in regions where external radiation should have evaporated them already, in particular in the ONC. Discs observed within 0.3 pc of the massive star  $\theta^1 C$  Ori are exposed to strong radiation fields ( $\sim 10^4 G_0$ , e.g. O’dell & Wen, 1994). The fact that there are still discs observed in the vicinity of the star suggest that either the discs were initially extremely massive ( $\gtrsim 1 M_{\odot}$ ), or that  $\theta^1 C$  Ori is younger than 0.1 Myr. Given that such massive discs are gravitationally unstable, and that the stellar age distribution in the ONC is  $\sim 1$  Myr (e.g. Da Rio et al., 2010, 2012), there must be other factors at play for these discs to have survived. Winter et al. (2019b) present a solution to this problem that consists of several mechanisms, one of them being extended periods of star formation. While the survival of discs in star forming regions with strong radiation background depends on a series of different factors, our results show that star formation that is sustained in time could be an

explanation for massive discs being detected in the vicinity of massive stars.

## 5 Summary and conclusions

We perform simulations of molecular cloud collapse and star formation. We begin with molecular clouds of mass  $10^4 M_\odot$  and a star formation efficiency of 30%. Star formation process ends when the star formation efficiency has been reached. The leftover gas is then removed instantaneously and the simulations continue. Stars with masses  $M_* \leq 1.9M_\odot$  have circumstellar discs, and massive stars ( $M_* > 1.9M_\odot$ ) emit UV radiation. The discs are subject to internal photoevaporation, external photoevaporation, dynamical truncations, and viscous evolution. We also implement a model for the evolution of dust inside the discs. We run the simulations for 2 Myr after the last star has formed. We conclude that:

1. Extended periods of star formation allow for relatively massive ( $M_{\text{gas}} \sim 100 M_{Jup}$ ,  $M_{\text{dust}} \sim 100 M_\oplus$ ) discs to survive the effects of photoevaporation.
2. The discs that make it to the end of our simulations are the ones that were born later (after  $\sim 4$  Myr) in the star formation process.
3. While photoevaporation removes gas from the discs, dust quickly becomes resistant to photoevaporation and the  $M_{\text{dust}}/M_{\text{gas}}$  ratio increases with time. This might allow discs to keep enough mass to form rocky planets, even when depleted of gas.
4. The presence of gas plays an important role in the survival of circumstellar discs, not just because it can absorb radiation from massive stars but also because it affects the dynamics of the regions.

Our results show that, while photoevaporation is clearly an important process in the depletion of disc masses, the complexity of disc and young star forming region evolution can provide the great variety observed in young disc populations.

## References

- Adams F. C., 2010, , 48, 47
- Adams F. C., Hollenbach D., Laughlin G., Gorti U., 2004, , 611, 360
- Adams F. C., Proszkow E. M., Fatuzzo M., Myers P. C., 2006, , 641, 504
- Anderson K. R., Adams F. C., Calvet N., 2013, , 774, 9
- Ansdell M., et al., 2016, , 828, 46
- Ansdell M., Williams J. P., Manara C. F., Miotello A., Facchini S., van der Marel N., Testi L., van Dishoeck E. F., 2017, , 153, 240
- Ansdell M., et al., 2020, arXiv:2010.00012 [astro-ph]
- Armitage P. J., 2000, , 362, 968
- Balog Z., Muzerolle J., Rieke G. H., Su K. Y. L., Young E. T., Megeath S. T., 2007, , 660, 1532
- Birnstiel T., Dullemond C. P., Brauer F., 2010, , 513, A79
- Bohlin R. C., Savage B. D., Drake J. F., 1978, , 224, 132
- Bontemps S., et al., 2001, ] 10.1051/0004-6361:20010474, 372, 173
- Breslau A., Steinhausen M., Vincke K., Pfalzner S., 2014, , 565, A130
- Cabrit S., Pety J., Pesenti N., Dougados C., 2006, , 452, 897

Carpenter J. M., Mamajek E. E., Hillenbrand L. A., Meyer M. R., 2006, , 651, L49

Cartwright A., Whitworth A. P., 2004, , 348, 589

Casertano S., Hut P., 1985, , 298, 80

Clarke C. J., 2007, , 376, 1350

Clarke C. J., Pringle J. E., 1991, *Monthly Notices of the Royal Astronomical Society*, 249, 588

Clarke C. J., Pringle J. E., 1993, *Monthly Notices of the Royal Astronomical Society*, 261, 190

Concha-Ramírez F., Vaher E., Portegies Zwart S., 2019a, , 482, 732

Concha-Ramírez F., Wilhelm M. J. C., Portegies Zwart S., Haworth T. J., 2019b, , 490, 5678

Concha-Ramírez F., Wilhelm M. J. C., Portegies Zwart S., van Terwisga S. E., Hacar A., 2020, arXiv e-prints, 2006, arXiv:2006.07378

Cuello N., et al., 2018, arXiv:1812.00961 [astro-ph]

Da Rio N., Robberto M., Soderblom D. R., Panagia N., Hillenbrand L. A., Palla F., Stassun K. G., 2010, *The Astrophysical Journal*, 722, 1092

Da Rio N., Robberto M., Hillenbrand L. A., Henning T., Stassun K. G., 2012, , 748, 14

Eisner J. A., Carpenter J. M., 2006, , 641, 1162

Eisner J. A., Plambeck R. L., Carpenter J. M., Corder S. A., Qi C., Wilner D., 2008, *The Astrophysical Journal*, 683, 304

Eisner J. A., et al., 2018, , 860, 77

Elmegreen B. G., Efremov Y., Pudritz R. E., Zinnecker H., 2000, *Protostars and Planets IV*, p. 179

Facchini S., Clarke C. J., Bisbas T. G., 2016, , 457, 3593

Falgarone E., Phillips T. G., 1991, 147, 119

Falgarone E., Phillips T. G., Walker C. K., 1991, *The Astrophysical Journal*, 378, 186

Fang M., et al., 2012, , 539, A119

Fatuzzo M., Adams F. C., 2008, , 675, 1361

Flaccomio E., Micela G., Sciortino S., 2012, *Astronomy and Astrophysics*, 548, A85

Font A. S., McCarthy I. G., Johnstone D., Ballantyne D. R., 2004, , 607, 890

Galli P. A. B., Bouy H., Olivares J., Miret-Roig N., Sarro L. M., Barrado D., Berihuete A., Brandner W., 2020, *Astronomy & Astrophysics*, 634, A98

Gorti U., Hollenbach D., 2009, , 690, 1539

Gorti U., Dullemond C. P., Hollenbach D., 2009, , 705, 1237–1251

Guarcello M. G., et al., 2016, arXiv:1605.01773 [astro-ph]

Habing H. J., 1968, *Bulletin of the Astronomical Institutes of the Netherlands*, 19, 421

Hacar A., Tafalla M., Forbrich J., Alves J., Meingast S., Grossschedl J., Teixeira P. S., 2018, , 610, A77

Hartmann L., 2002, *The Astrophysical Journal*, 578, 914

Haworth T. J., Boubert D., Facchini S., Bisbas T. G., Clarke C. J., 2016, , 463, 3616

Haworth T. J., Facchini S., Clarke C. J., Cleeves L. I., 2017, , 468, L108

Haworth T. J., Facchini S., Clarke C. J., Mohanty S., 2018a, , 475, 5460

Haworth T. J., Clarke C. J., Rahman W., Winter A. J., Facchini S., 2018b, , 481, 452

Hillenbrand L. A., Hartmann L. W., 1998, , 492, 540

Hollenbach D. J., Yorke H. W., Johnstone D., 2000, Protostars and Planets IV, p. 401

Jílková L., Portegies Zwart S., Pijloo T., Hammer M., 2015, , 453, 3157

Jílková L., Hamers A. S., Hammer M., Portegies Zwart S., 2016, , 457, 4218

Johnstone D., Hollenbach D., Bally J., 1998, , 499, 758

Kim J. S., Clarke C. J., Fang M., Facchini S., 2016, , 826, L15

Kraus A. L., Hillenbrand L. A., 2008, The Astrophysical Journal Letters, 686, L111

Kroupa P., 2001, , 322, 231

Krumholz M. R., Forbes J. C., 2015, Astronomy and Computing, 11, 1

Lada C. J., Lada E. A., 2003, , 41, 57

Larson R. B., 1995, Monthly Notices of the Royal Astronomical Society, 272, 213

Luhman K. L., 2007, , 173, 104

Luhman K. L., 2018, The Astronomical Journal, 156, 271

Luhman K. L., Esplin T. L., 2020, The Astronomical Journal, 160, 44

Luhman K. L., Mamajek E. E., 2012, , 758, 31

Luhman K. L., Esplin T. L., Loutrel N. P., 2016, , 827, 52

Lynden-Bell D., Pringle J. E., 1974, , 168, 603

Manara C. F., et al., 2020, arXiv:2004.14232 [astro-ph]

Mann R. K., Williams J. P., 2010, , 725, 430

Mann R. K., et al., 2014, , 784, 82

Neuhäuser R., Forbrich J., 2008, Handbook of Star Forming Regions, Volume II, p. 735

Nicholson R. B., Parker R. J., Church R. P., Davies M. B., Fearon N. M., Walton S. R. J., 2019,

O'dell C. R., 1998, , 115, 263

O'dell C. R., Wen Z., 1994, , 436, 194

Owen J. E., Ercolano B., Clarke C. J., Alexander R. D., 2010, , 401, 1415

Owen J. E., Clarke C. J., Ercolano B., 2012, , 422, 1880

Parker R. J., 2014, Monthly Notices of the Royal Astronomical Society, 445, 4037

Parker R. J., Alves de Oliveira C., 2017, Monthly Notices of the Royal Astronomical Society, 468, 4340

Parker R. J., Meyer M. R., 2012, , 427, 637

Pascucci I., et al., 2016, , 831, 125

- Pelupessy F. I., van der Werf P. P., Icke V., 2004, *Astronomy and Astrophysics*, 422, 55
- Pelupessy F. I., van Elteren A., de Vries N., McMillan S. L. W., Drost N., Portegies Zwart S. F., 2013, , 557, A84
- Petigura E. A., Howard A. W., Marcy G. W., 2013, *Proceedings of the National Academy of Science*, 110, 19273
- Pfalzner S., 2003, *The Astrophysical Journal*, 592, 986
- Pfalzner S., Vogel P., Scharwächter J., Olczak C., 2005a, *Astronomy and Astrophysics*, 437, 967
- Pfalzner S., Umbreit S., Henning T., 2005b, *The Astrophysical Journal*, 629, 526
- Pfalzner S., Tackenberg J., Steinhausen M., 2008, , 487, L45
- Picogna G., Ercolano B., Owen J. E., Weber M. L., 2019, , 487, 691
- Portegies Zwart S. F., 2016, , 457, 313
- Portegies Zwart S., McMillan S. L. W., van Elteren E., Pelupessy I., de Vries N., 2013, *Computer Physics Communications*, 183, 456
- Punzo D., Capuzzo-Dolcetta R., Portegies Zwart S., 2014, *Monthly Notices of the Royal Astronomical Society*, 444, 2808
- Reche R., Beust H., Augereau J.-C., 2009, , 493, 661
- Rodriguez-Merino L. H., Chavez M., Bertone E., Buzzoni A., 2005, , 626, 411
- Rodriguez J. E., et al., 2018, , 859, 150
- Rosotti G. P., Dale J. E., de Juan Ovelar M., Hubber D. A., Kruijssen J. M. D., Ercolano B., Walch S., 2014, , 441, 2094
- Rosotti G. P., Tazzari M., Booth R. A., Testi L., Lodato G., Clarke C., 2019, , 486, 4829
- Sacco G. G., et al., 2017, *Astronomy and Astrophysics*, 601, A97
- Scally A., Clarke C., 2001, , 325, 449
- Scalo J., 1990, ] 10.1007/978-94-009-0605-1-12, 162, 151
- Simon M., 1997, *The Astrophysical Journal Letters*, 482, L81
- Störzer H., Hollenbach D., 1999, , 515, 669
- Tobin J. J., et al., 2020, , 890, 130
- Trapman L., Rosotti G., Bosman A. D., Hogerheijde M. R., van Dishoeck E. F., 2020, arXiv:2005.11330 [astro-ph]
- Vicente S. M., Alves J., 2005, , 441, 195
- Vincke K., Pfalzner S., 2016, , 828, 48
- Vincke K., Pfalzner S., 2018, , 868, 1
- Vincke K., Breslau A., Pfalzner S., 2015, , 577, A115
- Wall J. E., McMillan S. L. W., Mac Low M.-M., Klessen R. S., Portegies Zwart S., 2019, arXiv e-prints, p. arXiv:1901.01132
- Williams J. P., Best W. M. J., 2014, , 788, 59

Williams J. P., Cieza L. A., 2011, , 49, 67

Williams J. P., Blitz L., McKee C. F., 2000, Protostars and Planets IV, p. 97

Winter A. J., Clarke C. J., Rosotti G., Booth R. A., 2018a, , 475, 2314

Winter A. J., Clarke C. J., Rosotti G., Ih J., Facchini S., Haworth T. J., 2018b, , 478, 2700

Winter A. J., Booth R. A., Clarke C. J., 2018c, , 479, 5522

Winter A. J., Clarke C. J., Rosotti G. P., 2019a, , 485, 1489

Winter A. J., Clarke C. J., Rosotti G. P., Hacar A., Alexander R., 2019b, , 490, 5478

Winter A. J., Kruijssen J. M. D., Chevance M., Keller B. W., Longmore S. N., 2020, , 491, 903

Wright N. J., Drake J. J., Drew J. E., Vink J. S., 2010, , 713, 871

Wright N. J., Parker R. J., Goodwin S. P., Drake J. J., 2014, Monthly Notices of the Royal Astronomical Society, 438, 639

van Terwisga S. E., Hacar A., van Dishoeck E. F., 2019, , 628, A85

van Terwisga S. E., et al., 2020, arXiv:2004.13551 [astro-ph]